Estimators for anticipating river meanders: a comparative study

Kai Qin* and Dylan A. Shell†

Department of Computer Science & Engineering,
Texas A&M University,
Technical Report #2017-2-1

February 24, 2017

Abstract

Increasingly, marine robots and unmanned surface vehicles will be deployed in rivers and riverine environments. The structure produced by flowing waters is worth investigating because it may be exploited for purposes of estimation, planning, and control. This report adopts a widely acknowledged model for the geometry of watercourse channels, namely sine-generated curves, as a basis for estimators that predict the shape of the yet unseen portion of the river. Predictions of this sort help a robot to choose actions which anticipate the future, for example, in throttling speeds to round a bend. After examining how to reparameterize standard filters to incorporate this model, we compare the performance of three Gaussian filters and show that nonideality and theoretical challenges (of non-linearity, multi-modality/periodicity) degrade the performance of standard Kalman filters very severely, but can be successfully mitigated by imposing an interval constraint. Thereafter, we present results of a constrained interval Kalman filter on data from three natural rivers. The results we report, including data from simulation, on map-based data, and on GPS positions collected from a boat on the Colorado river, show the effectiveness of our method on the estimation of meander parameters.

*Kai Qin (`kai.qin@nxp.com`) is with NXP Semiconductors.

†Dylan A. Shell (`dshell@cs.tamu.edu`) is with the Department of Computer Science and Engineering, Texas A&M University.

1 Introduction

Rivers have a degree of predictability that is important. The birth of civilization was, as we best understand it, critically linked to rivers and the regularity of their flooding. Still, the naïve impression of rivers as mostly straight watercourses is quite erroneous. As geologists Leopold and Langbein [4] write, "in fact, it is almost certain that the distance any river is straight does not exceed 10 times its width at that point." The fact that rivers do not erode to form straight lines, minimizing the source-to-sea distance, is a puzzle which remained a source of confusion for many years. The question attracted the attention of no less than Einstein, who, in 1926, clarified the process of river bank erosion (and the related paradox of loose tea leaves moving to the center of a stirred cup), overturning the accepted model at that time [2]. It is now understood that meanders are no accident but that they form because the river does the least work in snaking along its course, turning first this way, then that, many times.

Inevitably, as more and more applications are conceived, autonomous surface vehicles will advance beyond open water scenarios to be deployed more widely. Rivers and riverine environments present many interesting and important opportunities because they are arteries carrying fresh water—a precious and all-too-scarce resource; because they are sites of ecological diversity—including unique fauna and flora; and because they are corridors of commerce—several rivers are of especial historical and cultural significance. But streams and rivers pose significant difficulties too. As Synder et al. [8] observe "prior map information on water hazards and obstacles is not dependable and does not have the accuracy needed for precision navigation and sensor directed reconnaissance." Meanders, in particular, present challenges because they hamper long-distance observation and occlusion increases uncertainty. Inevitably, watercraft navigating a river for the first time have only limited understanding of stretches of water lying ahead.

Fortunately, meandering rivers possess considerable regularity: meanders have been shown to be well-characterized by a sine-generated curve, of which the angular direction at any point with respect to the mean down-valley direction is a sine function of the distance measured along the channel [4]. This report explores how this model can serve as the foundation for estimators that fuse observations to make predictions of the shape of unseen portions of the river (see Fig. 1). Essentially, the model provides a parsimonious state space over which our filters operate, this representational economy being translated into efficiency. The output of the estimation process is valuable for making control decisions, for example, in selecting reference trajectories or paths for a controller to track, or, more simply, in imposing velocity bounds to slow down the vehicle as it approaches a bend. Predictions of river geometry can provide rich information especially when combined with other domain knowledge. A great deal that is useful for navigation can be gleaned, as illustrated by the following passage:

> "River boatmen navigating upstream on a large river face the problem that the deepest water, which they usually prefer, tends to coincide with

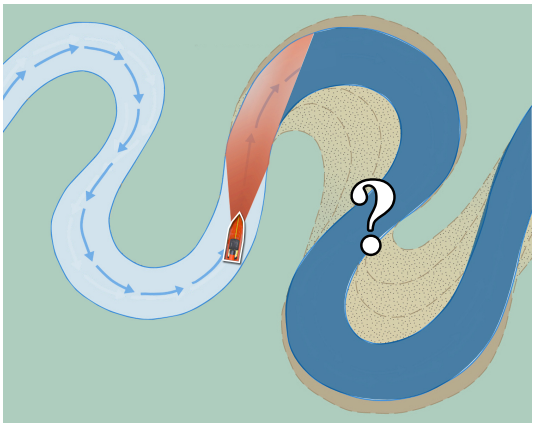

Figure 1: This report formulates and compares estimators that model river meanders to predict the shape of the channel ahead of the robot. Such estimates could be helpful in choosing the appropriate throttle to apply in rounding the next bend, or in picking trajectories for the controller to track.

> the streamline of highest velocity. Their solution is to follow the *thalweg* (the deepest part of the river, from the German for 'valley way') where it crosses over the center line of the channel as the channel changes its direction of curvature but to cut as close to the convex bank as possible in order to avoid the highest velocity near the concave bank." [4]

As readers may anticipate, the periodic nature of the model presents some challenges for a standard extended Kalman filter. Indeed this *is* the case and, as will be clearly shown, these issues affect performance in practice. Our first step was to adopt a parameterization of meander geometry (Section 3) and then to seek an understanding of how classical Gaussian filters would behave using the model. This examination, which we report in Section 4.1, involved comparison of the performance of three Gaussian filters in tracking and predicting the river's centerline. It led us to recognize the importance of constraints on the state space to ensure the estimate is confined to a single period, guaranteeing unimodality. Thereafter, we investigated the performance of this superior, constrained filter on data from three natural rivers in detail (Sections 4.2–5). In the next section, however, we discuss relationships to the relevant literature.

2 Related work

2.1 Models of river meanders

Langbein and Leopold [4] first proposed the sine-generated curve model of river meanders, formalized as:

$$\theta(s) = A \sin\left(\frac{2\pi s}{M}\right), \tag{1}$$

where $\theta(s)$ is the angle in radians between the direction of flow and the mean down-valley direction. The mean down-valley direction is a reference axis oriented along the centerline of the meandering pattern, pointing downstream; as the name indicates, it reflects the broad slope of the land. Note that $\theta(s)$ is a function of the maximum angle A in radians, spatial period per meander M in meters and s, which is the distance along river from the apex of a left-hand bend in meters. This form was proposed because it minimizes the sum of squares of change in direction and also total work in bending.

Thereafter, Thakur and Scheidegger [10] examined the statistical distribution of angles of deviation with the mean down-valley direction. They confirmed that the angles of deviation in river courses are normally distributed. Their evidence provides support for the sine-generated curve model and also hints toward its aptness as a representation for estimation.

Much more recently, Mecklenburg and Jayakaran [5], to sidestep the highly nonlinear sine-generated curve, proposed a new arc-and-line meander pattern that represents the meander pattern with connecting arcs and lines; such a model, while perhaps easier to fit to geological data, does not provide an obvious state space description—unfortunately making it rather more complicated for our purposes.

2.2 Estimators from a constrained vs. unconstrained optimization perspective

A vast panoply of Bayesian filters have been proposed for parameter estimation. The present report, being the first we are aware of to study the meander problem, begins by applying standard estimation techniques. The Kalman filter, a parametric recursive estimator for systems with Gaussian uncertainty, seems like a good choice, especially given that a Gaussian distribution is reported in [10]. However, as the meander problem is not linear, we must turn to various progeny of the classical Kalman filter.

For nonlinear systems, the extended Kalman filter (EKF) and the unscented Kalman filter (UKF) are the most commonly used Gaussian filters. The EKF linearizes system dynamics using the first term of the Taylor series expansion, which requires the calculation of Jacobians or Hessians. The UKF approximates the state distribution by generating weighted samples, or so-called *sigma points*, deterministically from the state distribution [3]. Both filters, at each iteration, are two-step estimators that include a prediction step and a measurement update step. Compared to the EKF, the UKF has comparable computational complexity while being shown to yield more accurate results, at least to the second order of the Taylor series expansion [1]. In the prediction step, the EKF propagates the previous state estimates through linearized system dynamics. On the other hand, the UKF first generates sigma points from the previous state estimates and then propagates them into the system dynamics. The measurement update step of both filters is a correction of the predicted state estimates from the measurements. Though seldom seen this way, measurement update steps of

both filters can be regarded as the solution of an unconstrained optimization problem [13].

Constraints can be introduced, for example, to impose a restriction on parts of the state space; this leads to constraint Kalman filters, which have been formulated to integrate additional information of the system into the filter design. A comprehensive literature review of Kalman filter and its extensions with state constraints can be found in [7] and [9]. Constraint Kalman filters can be classified into linear and nonlinear types according to the linearity of the system transition function and measurement function. Based on the types of constraints, there are equality and inequality constraint filters.

The unscented recursive nonlinear dynamic data reconciliation (URNDDR) filter [12] improves the way that the EKF obtains the updated state estimates by solving (numerically) a constrained optimization problem and updates the state covariance by selecting sigma points and weights like the UKF does. But, additionally, URNDDR solves a constrained optimization problem to ensure that any state inequality constraints are satisfied in the sigma point updates too. Taken together, both the updated state estimate and error covariance will satisfy state space constraint. Unfortunately, this comes at a substantial cost: URNDDR needs much more computation than the UKF and is sensitive to the performance of the constrained optimization problem solver. For a four-dimensional state space, at each iteration, it needs to run the solver nine times and, moreover, estimation terminates when the solver fails to find a solution.

A practical solution, and one which we adopt, is proffered by the constraint interval unscented Kalman filter (CIUKF) of Teixeira et al. [9]. It uses the same method as URNDDR for the selection of $2n+1$ sigma points $\chi_{j,k-1}$ and weights $\gamma_{j,k-1}$, where n is the dimension of the state space and $j = 0, \ldots, 2n$.

Equations (2) to (7) are used to generate sigma points that satisfy the interval constraints, $x_L \leq \chi_{j,k-1} \leq x_U$.

$$\chi_{0,k-1} = \hat{x}_{k-1|k-1}, \tag{2}$$

$$\chi_{j,k-1} = \hat{x}_{k-1|k-1} + \alpha_{j,k-1}\mathrm{col}_j[(P^{xx}_{k-1|k-1})^{\frac{1}{2}}] \quad \text{for } j = 1, \ldots, n, \tag{3}$$

$$\chi_{j,k-1} = \hat{x}_{k-1|k-1} - \alpha_{j,k-1}\mathrm{col}_j[(P^{xx}_{k-1|k-1})^{\frac{1}{2}}] \quad \text{for } j = n+1, \ldots, 2n, \tag{4}$$

where for $i = 1, 2, \ldots, n$ and $j = 1, \ldots, 2n$:

$$\alpha_{j,k-1} = \min(\mathrm{col}_j(\beta)) \tag{5}$$

$$\beta_{(i,j)} = \begin{cases} \sqrt{n+\lambda} & \text{if } \Gamma_{(i,j)} = 0, \\ \min\left(\sqrt{n+\lambda}\,, \frac{x_{U,i} - \hat{x}_{i,k-1|k-1}}{\Gamma_{(i,j)}}\right) & \text{if } \Gamma_{(i,j)} > 0, \\ \min\left(\sqrt{n+\lambda}\,, \frac{x_{L,i} - \hat{x}_{i,k-1|k-1}}{\Gamma_{(i,j)}}\right) & \text{if } \Gamma_{(i,j)} < 0, \end{cases} \tag{6}$$

$$\Gamma = \left[\ (P^{xx}_{k-1|k-1})^{\frac{1}{2}} - (P^{xx}_{k-1|k-1})^{\frac{1}{2}}\ \right]. \tag{7}$$

The weights corresponding to χ_{k-1} are calculated as, for $j = 1, \ldots, 2n$:

$$\gamma_{0,k-1} = b_{k-1},\ \gamma_{j,k-1} = c_{k-1}\alpha_{j,k-1} + b_{k-1}, \tag{8}$$

where

$$c_{k-1} = \frac{2\lambda - 1}{2(n+\lambda)\left(\sum_{j=1}^{2n} \alpha_{j,k-1} - (2n+1)\sqrt{n+\lambda}\right)}, \tag{9}$$

$$b_{k-1} = \frac{1}{2(n+\lambda)} - \frac{2\lambda - 1}{(2\sqrt{n+\lambda})\left(\sum_{j=1}^{2n} \alpha_{j,k-1} - (2n+1)\sqrt{n+\lambda}\right)}. \tag{10}$$

The constrained sigma points are then propagated through system transition function $f(\chi_{j,k-1}, u_k)$ to obtain the predicted sigma points $\chi_{j,k}$, where u_k is the control vector at state k.

$$\chi_{j,k} = f(\chi_{j,k-1}, u_k) \quad \text{for} \quad j = 0, \ldots, 2n \tag{11}$$

$$\hat{x}_{k|k-1} = \sum_{j=0}^{2n} \gamma_{j,k-1}\chi_{j,k} \tag{12}$$

$$P^{xx}_{k|k-1} = \sum_{j=0}^{2n} \gamma_{j,k-1}[\chi_{j,k} - \hat{x}_{k|k-1}][\chi_{j,k} - \hat{x}_{k|k-1}]^{\mathsf{T}} + Q_k \tag{13}$$

Equations (12) and (13) are for computing the predicted parameters state estimate $\hat{x}_{k|k-1}$ and its error covariance matrix $P^{xx}_{k|k-1}$.

$$\chi^*_{0,k} = \hat{x}_{k|k-1} \tag{14}$$

$$\chi^*_{j,k} = \hat{x}_{k|k-1} + \sqrt{n+\lambda}\,\mathrm{col}_j[(P^{xx}_{k|k-1})^{\frac{1}{2}}] \quad \text{for } j = 1, \ldots, n \tag{15}$$

$$\chi^*_{j,k} = \hat{x}_{k|k-1} - \sqrt{n+\lambda}\,\mathrm{col}_j[(P^{xx}_{k|k-1})^{\frac{1}{2}}] \quad \text{for } j = n+1, \ldots, 2n \tag{16}$$

Based on the predicted parameters state estimate, (14)–(16) are used to calculate unconstrained sigma points $\chi^*_{j,k}$ as in standard UKF.

$$Y_{j,k} = h(\chi^*_{j,k}) \text{ for } j = 0, \ldots, 2n \tag{17}$$

$$\hat{y}_{k|k-1} = \sum_{j=0}^{2n} \gamma_{j,k-1} Y_{j,k} \tag{18}$$

$$P^{yy}_{k|k-1} = \sum_{j=0}^{2n} \gamma_{j,k-1} \left[Y_{j,k} - \hat{y}_{k|k-1}\right] \left[Y_{j,k} - \hat{y}_{k|k-1}\right]^{\mathsf{T}} + R_k \tag{19}$$

$$P^{xy}_{k|k-1} = \sum_{j=0}^{2n} \gamma_{j,k-1} \left[\chi_{j,k} - \hat{x}_{k|k-1}\right] \left[Y_{j,k} - \hat{y}_{k|k-1}\right]^{\mathsf{T}} \tag{20}$$

$$K_k = P^{xy}_{k|k-1}(P^{yy}_{k|k-1})^{-1}. \tag{21}$$

In (17), predicted observation sigma points Y_k are computed from unconstrained sigma points $\chi^*_{j,k}$. Predicted observation $\hat{y}_{k|k-1}$ and its error covariance matrix are calculated in (18) and (19). Cross-variance between parameters and observation $P^{xy}_{k|k-1}$ is computed in (20). Kalman gain K_k is then calculated in (21). Finally, the mean and error covariance matrix of the updated state estimate are obtained by (22) and (23), where $\bar{\theta}_k$ is the measurement at state k:

$$\begin{aligned} \hat{x}_{k|k} \quad = \quad & \underset{\{x_k\}}{\arg\min} \Big[(\bar{\theta}_k - h(x_k))^{\mathsf{T}} (R_k)^{-1} (\bar{\theta}_k - h(x_k)) + \\ & (x_k - \hat{x}_{k|k-1})^{\mathsf{T}} (P^{xx}_{k|k-1})^{-1} (x_k - \hat{x}_{k|k-1}) \Big], \end{aligned} \tag{22}$$

subject to the following constraints: $x_L \leq x_k \leq x_U$,

$$P^{xx}_{k|k} = P^{xx}_{k|k-1} - K_k P^{yy}_{k|k-1} K_k^{\mathsf{T}}. \tag{23}$$

Above, (22) solves the constrained optimization problem only for the sampled mean of the state distribution, instead of solving $2n+1$ constrained optimization problems for $2n+1$ updated sigma points. Thus, as a result, the CIUKF opts to weaken the constrained requirement for variances compared to the URNDDR method. It, instead, uses the standard UKF method as in (23) to obtain the state covariance.

3 Formulation and approach

Estimating meander parameters using the model in (1) requires the robot to measure the mean down-valley direction and to start at the apex of a left-hand bend. Such requirements are excessively unreasonable for autonomous vehicles and are limiting, if they cannot be overcome. By including offset and scaling parameters, we introduce a new function for the river's centerline:

$$\theta(s) = A \sin(Bs + C) + D, \tag{24}$$

where s is the distance along the river from the robot's initial location; $\theta(s)$ is the angle between the direction of flow and magnetic East in radians; A is the maximum angle in radians; B is the spatial frequency in radians per unit length; C is the phase shift in radians; D is the angle between the mean down-valley direction and magnetic East. In addition to the spatial frequency B, the spatial period M is computed as:

$$M = \frac{2\pi}{B}. \tag{25}$$

Fig. 2 shows a illustration of the parameters A, D and M.

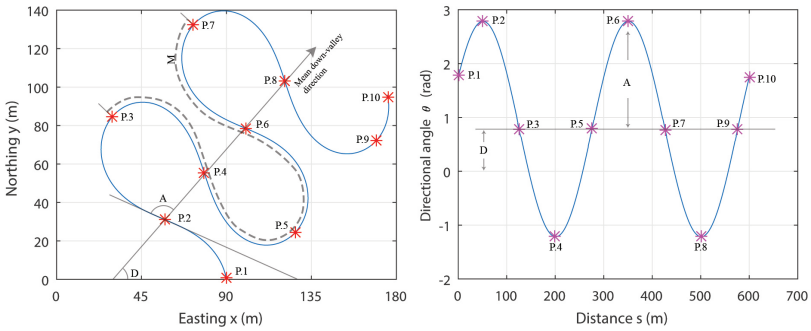

Figure 2: Illustration of the parameters A, D and M.

3.1 Problem Formulation

Consider a river meander centerline that is well-characterized by the following sine-generated curve in a Cartesian coordinate system:

$$y_1(s) = \int_0^s \cos(\theta(\tau))\, d\tau + y_1(0), \tag{26}$$

$$y_2(s) = \int_0^s \sin(\theta(\tau))\, d\tau + y_2(0), \tag{27}$$

$$\theta(s) = A\sin(Bs + C) + D. \tag{28}$$

Collecting A, B, C and D into a single parameter vector to be estimated, we define the state describing the river as:

$$x = \begin{bmatrix} A & B & C & D \end{bmatrix}^{\mathsf{T}}. \tag{29}$$

We assume that the robot is equipped with sensors that can measure the coordinates $(y_1(k), y_2(k))$ of locations along the river's centerline, a distance s_k along river from an initial point $(y_1(0), y_2(0))$, and the angle $\theta_k \in [-\pi, \pi)$ between the direction of flow and magnetic East, where the subscript k denotes the k^{th} measurement. To simplify this problem, the measurements of s_k (distances along the river) are treated as perfect and, therefore, $s_k \leq s_{k+1}$. We are concerned with θ at s_k, but of which only an imperfect observation, denoted $\bar{\theta}_k$, can be made; we assume that its error, v_k, is normally distributed with zero mean and variance R_k. Since we are assuming measurements of the watercourse centerline, nothing need be assumed about the river width.

We desire an estimate of the parameters x_k at a point $(y_1(k), y_2(k))$ given spatially discrete sensor readings. With these definitions in place, at each state k the river meander estimation problem is formulated as follows.

3.2 Filter Design

The sine-generated curve model exhibits nonlinearity in three of the four parameters $[A\ B\ C\ D]^{\mathsf{T}}$, none of which are directly observable. Nevertheless, we wish

PROBLEM 1: **River Meander Estimation**

Input: Prior belief of state $\mathcal{N}(\hat{x}_{k-1},\ P_{k-1})$
Input: An observation $\mathcal{N}(\bar{\theta}_k,\ R_k)$
Input: Distance s_k along the centerline from initial point
Output: Posterior belief of state $\mathcal{N}(\hat{x}_k,\ P_k)$

to enable the robot to estimate these parameters in real-time. The non-linearity precludes a standard Kalman filter, so we began by implementing EKF and UKF solutions.

The prior studies by geologists treat the sinusoidal parameters as fixed constants over the region of the river under study. We expect that over long distances these parameters may drift but, as we have no *a priori* transition model for any of the four variables, we assume constant parameters for each river. Of course, if other information is known it can be incorporated too; we have:

$$x_k = T x_{k-1} + \mu_k \tag{30}$$

where the transition matrix T is the $4{\times}4$ identity matrix I. To account for gradual drift in the values, it is prudent to add system process noise $\mu_k \sim \mathcal{N}(0, Q_k)$ to the state transition equation, where Q_k is the process-noise covariance matrix. (We have Q_k as a diagonal matrix, because error of each parameter is assumed to be independent.)

For the measurement update step of the filter, we choose the meander direction angle $\bar{\theta}_k$ as the (sole) observed variable because it has been confirmed to be normally distributed [10]. Perhaps the obvious alternative, using the Cartesian coordinates of points on the meander centerline, does not have this statistical property and, moreover, the measurement model for the coordinates (equations (26), (27)) is complicated. In contrast our measurement function is given by:

$$\bar{\theta}_k = h(x_k, s_k) = A\sin(Bs_k + C) + D + v_k, \tag{31}$$

where $v_k \sim \mathcal{N}(0,\ R_k)$ is the measurement error. The Jacobian matrix H_k for the observation model is given as:

$$\begin{aligned} H_k &= \left.\frac{\partial\theta(s)}{\partial x_k}\right|_{x_k=\hat{x}_{k|k-1}, s=s_k} \\ &= \begin{bmatrix} \sin(Bs_k + C) & AB\cos(Bs_k + C) \\ A\cos(Bs_k + C) & 1 \end{bmatrix}. \end{aligned} \tag{32}$$

Since Kalman filters, along with various extensions thereto, represent belief over their state space with a multivariate normal distribution, they can do poorly (even breaking down) when the distribution is not unimodal [11]. Regrettably, the state space distribution of meander parameters is not unimodal. The periodic nature of sine functions poses a problem: even exact observations could confirm an infinite number of values. For example, parameters $[A\ B\ C\ D]^\mathsf{T}$ and

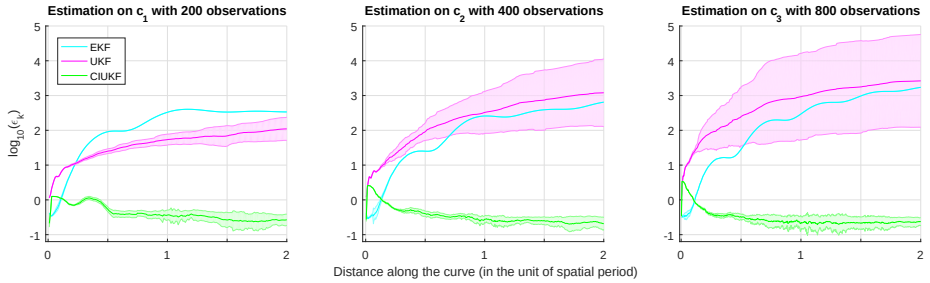

Figure 3: State weighted error of constraint interval unscented Kalman filter *vs.* Number of measurements. The EKF and UKF produce estimates that are divergent. Plots show estimates of mean and variance computed from 30 independent simulations for each filter. Measurements are made every 5 m, though the three curves are of different scales. The horizontal axis is in units of the ground truth curve's spatial period.

$[A\ B\ (C + 2n\pi)\ D]^\mathsf{T}$ represent the same sine-generated curve for any integer number n. The probabilistic analogue, thus, has multiple modes. These infinite modes make it impossible to approximate the state distribution as a single Gaussian or a Gaussian Mixture [6]. We approach this problem by using the CIUKF to incorporate the fact that it is unimodal when parameters are constrained inside a single period (for a proof of unimodality, given the constraints, refer to the Appendix).

We implement a CIUKF based on the algorithm given in [9] and the system dynamics in (30) and (31). The *posteriori* state estimate $\hat{x}_k$ is computed by solving the constrained optimization problem described in the following equation numerically:

$$\begin{aligned}\hat{x}_k = \underset{\{x_k\}}{\arg\min} \Big[&(\bar{\theta}_k - h(x_k, s_k))^\mathsf{T} (R_k)^{-1} (\bar{\theta}_k - h(x_k, s_k)) + \\ &(x_k - \hat{x}_{k|k-1})^\mathsf{T} (P^{xx}_{k|k-1})^{-1} (x_k - \hat{x}_{k|k-1}) \Big] \\ &\text{subject to: } x_L < x_k \leq x_U, \end{aligned} \tag{33}$$

where the observation model is given in (31).

4 Results

This section reports measures of the performance of the estimators in three separate evaluations. In Section 4.1, we first consider a simulated setting where the ground truth is both known and is a true sine-generated curve. Since the true parameters are known, we can measure error of the estimate exactly. Even in these circumstances that are much simpler than customarily encountered, the EKF and UKF leave much to be desired. The second and third evaluations

involve estimation on river meanders using map-based data (Section 4.2) and GPS positions collected from a boat (Section 4.3). Of course, these meanders are only approximately characterized by the sine-generated curve model, but the data show that the CIUKF is able to provide useful predictions for the robot nevertheless.

4.1 Evaluation on sine-generated curves

For real rivers, one determines the scale of a meander from its spatial period M. The longer the spatial period, the larger the scale of the meander. Leopold and Langbein [4] presented the data collected from two meanders of the Mississippi River near Greenville, Mississippi (USA) and the Blackrock Creek in Wyoming (USA) to illustrate their model. Comparing the meander of the Mississippi River has spatial period of about 20 miles, while Blackrock Creek is of much smaller scale with a period of 700 feet. Here, we choose three curves with different spatial period to examine the filter performance of estimations on meanders with different scales.

Comparisons of performance of the EKF, UKF and CIUKF on sine-generated curves c_1, c_2, c_3, of which the ground truth parameters are:

$$x_{c_1} = \begin{bmatrix} 1 & \frac{2\pi}{500} & \frac{2\pi}{3} & \frac{\pi}{4} \end{bmatrix}^{\mathsf{T}}, \tag{34}$$

$$x_{c_2} = \begin{bmatrix} 1 & \frac{2\pi}{1000} & \frac{2\pi}{3} & \frac{\pi}{4} \end{bmatrix}^{\mathsf{T}}, \tag{35}$$

$$x_{c_3} = \begin{bmatrix} 1 & \frac{2\pi}{2000} & \frac{2\pi}{3} & \frac{\pi}{4} \end{bmatrix}^{\mathsf{T}}. \tag{36}$$

The initial state and its covariance matrix are given as

$$\beta_0 = [\pi/2 \quad \frac{2\pi}{1500} \quad \pi/2 \quad \pi/2]^{\mathsf{T}}, \tag{37}$$

$$P_0 = \begin{bmatrix} 1 & 0 & 0 & 0 \\ 0 & 0.01 & 0 & 0 \\ 0 & 0 & 1 & 0 \\ 0 & 0 & 0 & 1 \end{bmatrix}. \tag{38}$$

The measurement covariance matrix R, the process covariance matrix Q, and the sampling distance Δs, i.e., the distance between two sequential measurements, are initialized as

$$R = \frac{\pi}{6}, \tag{39}$$

$$\Delta s = 5\ m, \tag{40}$$

$$Q = 0. \tag{41}$$

The CIUKF lower and upper limits, x_L and x_U, were

$$x_L = [0\ 0\ 0\ 0]^{\mathsf{T}} \quad \text{and} \quad x_U = [2.2\ 0.1\ 2\pi\ 2\pi]^{\mathsf{T}}. \tag{42}$$

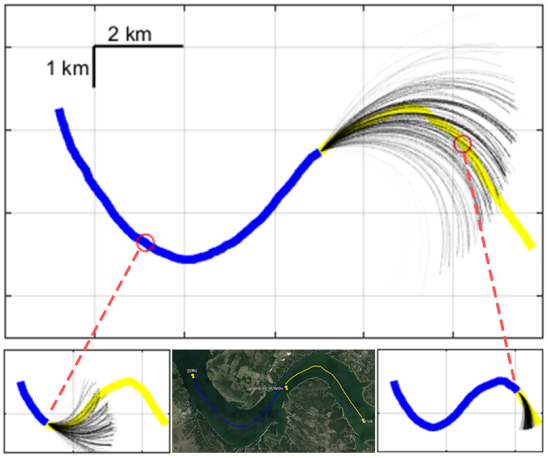

Figure 4: After taking measurements (shown in blue) part of the way along the Brazos River, 100 samples are drawn randomly from the CIUKF estimator's current state distribution. Main image takes samples up to 8995 m from the designated start, lower-left up to 3975 m, and lower-right takes 12 957 m. These are plotted forward from this point to show predictions for the still unseen portion of the river. The curve in yellow is the river's actual centerline that the robot has not observed yet. Transparency corresponds to normalized probability of the sample.

The upper limit for parameter A was selected to be 2.2 rad because the sine-generated curve model generates meanders with closed loops for values of A above approximately 2.2 rad, cf. [5]. And the upper limit for B is set to 0.1 m/rad, since we ignore the meanders with spatial period less than 62.83 m. Error corrupted observation is introduced to the filter by adding zero mean Gaussian error with standard deviation of $\pi/18$ rad to the true measurements.

For all estimation results reported in this report, the filters were initialized as described in this scenario, except that for real data, no additional Gaussian noise was added to the measurements, nor is the sampling distance treated as fixed.

A standard measure of performance in literature on the Kalman filters and its extensions [7,9] is the root-mean-square error (RMSE) of each state. However, we found it necessary to adopt a different indicator because the spatial frequency parameter, B, has a much smaller order than the other parameters, especially for large-scale meanders, yet affects the quality of predictions rather acutely. We decided instead to use the weighted error of the estimated parameters, defined

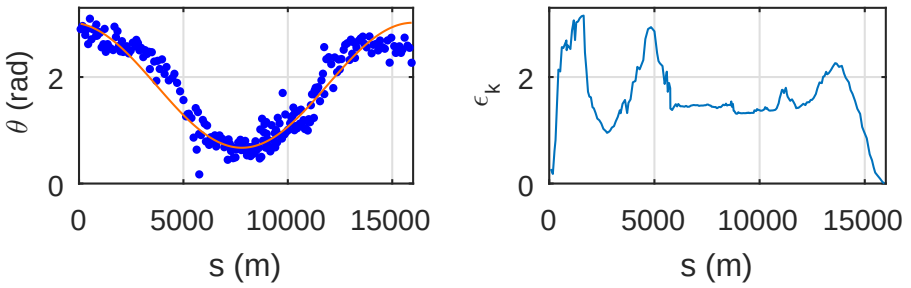

Figure 5: Plots showing estimation quality of CIUKF on the Brazos River data. Left: (a) Blue dots are data points and the solid orange line shows the estimator's fit after 225 measurements. Right: (b) State weighted error calculated as data arrive (error estimated with all measurements used as ground truth).

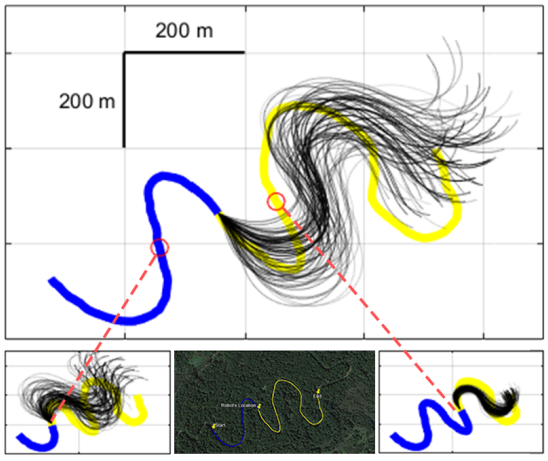

Figure 6: An analogous plot to that of Fig. 4 but for the L'Anguille River. It is a substantially smaller watercourse. In the main image the samples are drawn after 647 m, for the lower-left after 369 m, and for the lower-right after 991 m.

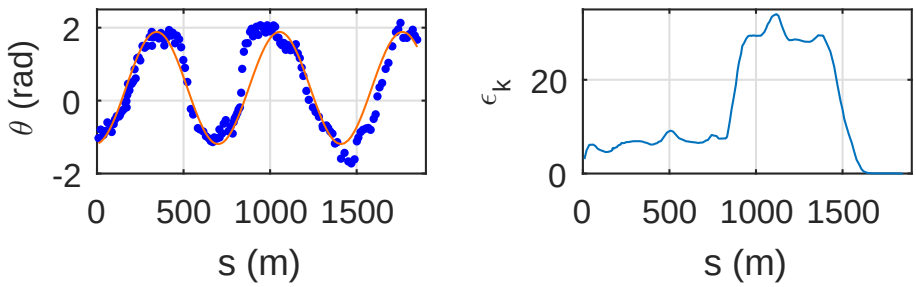

Figure 7: An analogous plot to that Fig. 5 but for the smaller L'Anguille River. Left: (a) Blue dots are data points and the solid orange line shows the estimator's fit after 159 measurements. Right: (b) State weighted error calculated as data arrive (error estimated with all measurements used as ground truth).

as

$$\epsilon_k = (\hat{x}_k - x_{c_i})^{\mathsf{T}} (P_k)^{-1} (\hat{x}_k - x_{c_i}), \tag{43}$$

where x_{c_i} denotes the ground truth for the sine-generated curves. The similarity between (33) and (43) is worth clarifying: the measurement update steps of all three filters can be regarded as the solution of an optimization problem, for which the objective function is simply weighted least squares [13]. The first term in (33) is concerned with the immediate sensor reading; we discard its contribution and the second term forms the basis of the state weighted error metric, as it uses the same matrix, P_k^{-1}, for the weights.

Representative results using the three filters on the curves appear in Fig. 3, which shows mean and variances summarizing 30 independent simulations per filter. The vertical axis is the logarithm (base 10) of weighted error of estimated parameters at each state. The horizontal axis shows the observation data set for each curve, for twice the spatial period of each curve, with measurements with an inter-sample distance of 5 m. The convergence of CIUKF's stands in clear contrast to the degradation of the estimates of both the EKF and UKF.

4.2 Evaluation on map-based data

The verisimilitude of the sine-generated model will always be imperfect for real rivers. In a sense, the preceding evaluation gives best possible conditions for an estimator and, thus, gives ample justification to dispense with the EKF and UKF further.

In order to provide realistic river data as input to the CIUKF, we manually labeled rivers on maps within Google Earth. Longitudes and latitudes of points on two centerlines of the Brazos River near Lake Whitney, Texas (USA) and the L'Anguille River near Caldwell, Arkansas (USA) were collected and processed to provide measurements for the filter. Satellite photographs of these two meanders are shown in lower-center insets in Fig. 4 and Fig. 6.

As before, we purposefully used input data at different scales. The total distances traversed in the datasets for the rivers are 15 929 m and 1849 m, respectively. There are 225 labeled points with average sampling distance of 70 m for the meander centerline of the Brazos River, and 159 labeled points with average sampling distance of 11 m for the meander centerline of the L'Anguille River. Fig. 5(a) and Fig. 7(a) show the measured and the CIUKF estimated directional angles of both meanders, where the angles are computed using (24) and red line is plotted using the estimated parameters after the final measurement. In order to track the performance of the filter over the distance along the flow, we have constructed the weighted error at each state, see Fig. 5(b) and Fig. 7(b), using (43), where here parameters estimated after all measurements is taken to be the ground truth in lieu of any alternative.

A more direct and perhaps a more meaningful visualization of the estimate is to produce sine-generated curves using sampled parameters from the estimator, and convert those into Universal Transverse Mercator (UTM) coordinates. Fig. 4 and Fig. 6 show predictions of the river forward of where the robot has traveled. Fig. 4 shows the visualization of estimates at 3975 m (lower-left inset), 8995 m (main figure) and 12 957 m (lower-right inset). Fig. 6 shows the visualization of estimates at 369 m (lower-left inset), 647 m (main figure) and 991 m (lower-right inset). The transparency of predicted meanders indicates the normalized probability densities of the samples.

4.3 Evaluation using data collected on a boat

To further get a sense of how capable the estimator would be for use on a robot, we used data collected *in situ* from a boat navigating an extended stretch of river. We hired a ski-boat (along with an experienced pilot) and collected GPS positions of the boat trajectory on the Colorado River starting from noon, 4^{th} Sept. 2016. To get an overall sense of the entire dataset, Fig. 10 shows the trajectory tracked on our homeward leg, returning from the furthest point reached back to the dock, with a distance of 40 593 m. The entire trip was twice this one-way length, for which we made 8366 measurements with an average sampling distance of 10 m. The measurement frequency for the GPS sensor was 10 Hz. The average speed for the boat was 10 m/s, though the boat is capable of a maximum speed roughly double that.

Turning first to data collected on the outward journey, we applied CIUKF using parameters identical to before on the first stretch of 14 900 m for which there are 1370 measurements with average sampling distance of 10 m. Fig. 8 provides a visualization of estimates at 5020 m (lower-left inset), 9651 m (main figure) and 12 030 m (lower-right inset) on the outward journey. The filter fits a sinusoidal curve to the measurements in a manner comparable to previous data. Fig. 8 shows additional detail on convergence for this part of the journey. However, in the next the section, we apply the filter over a longer stretch of the Colorado River, with a far less satisfactory outcome.

We are also interested in situations where the boat does not to follow the centerline exactly owing to uncertainty. To simulate this situation we corrupted the

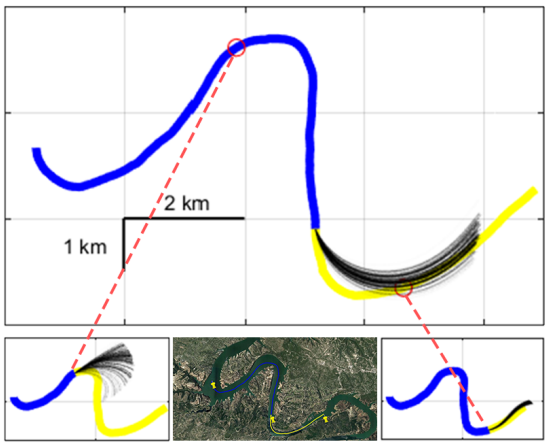

Figure 8: Plots analogous to those in Figs. 4 & 6 for data collected from GPS in a boat on the Colorado River. In the main image the samples are drawn after 5020 m, for the lower-left after 9651 m, and for the lower-right after 12 030 m.

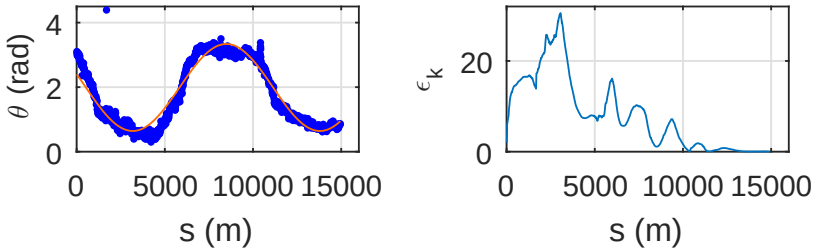

Figure 9: Plots analogous to those in Figs. 5 & 7 for GPS data from the boat on the Colorado River. Left: (a) Blue dots are data points and the solid orange line shows the estimator's fit after 1370 measurements. Right: (b) State weighted error calculated as data arrive (error estimated with all measurements used as ground truth).

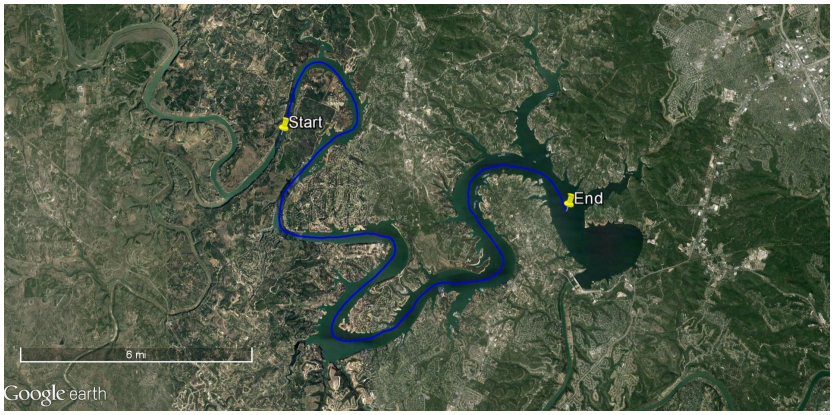

Figure 10: The trajectory the boat travelled on the Colorado River, TX (USA).

GPS positions with noise through the addition of random displacements. Vectors v_d, in polar coordinates (r_{v_d}, θ_{v_d}), are randomly drawn from distributions $r_{v_d} \sim \mathcal{N}(20, 25)$ and $\theta_{v_d} \sim \mathcal{U}(0, 2\pi)$. The mean value of the displacement magnitude, 20 m, is inappreciable compared to the length and width of the meander. Nevertheless, Fig. 11 (a) shows that the added displacement vectors introduce non-negligible errors into the estimate of direction. As shown in Fig. 11 (b), it also takes more steps for the CIUKF to converge. In our experiments, the boat's skipper may have deviated from the true river centerline, but one would expect that the error introduced by an experienced pilot would be less than the noise introduced synthetically in the preceding evaluation.

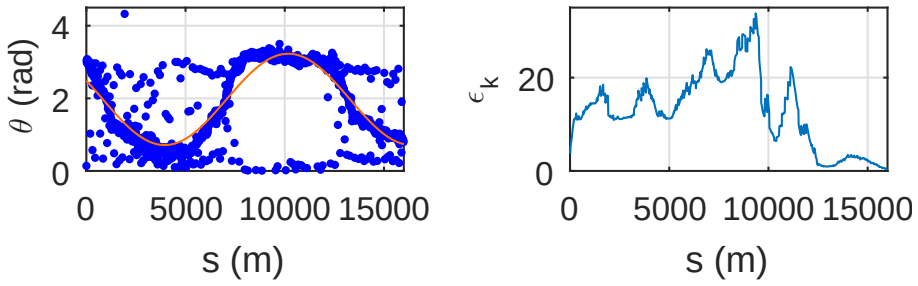

Figure 11: Plots analogous to those in Figs. 5, 7 & 9 for GPS data from the boat on the Colorado River, but with noise added. Left: (a) Blue dots are data points and the solid orange line shows the estimator's fit after 1370 measurements. Right: (b) State weighted error calculated as data arrive (error estimated with all measurements used as ground truth).

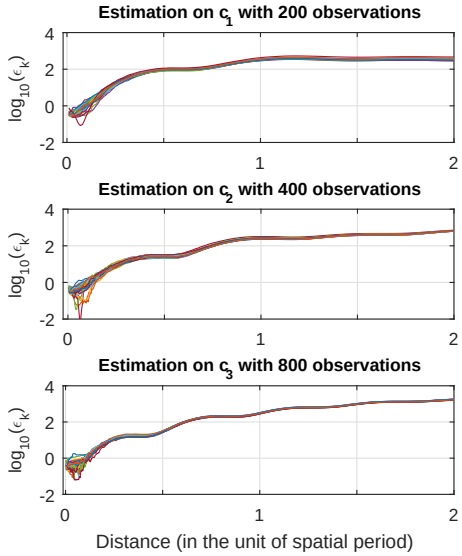

Figure 12: State weighted error of predictions made by the EKF. The horizontal axis is in units of the ground truth curve's spatial period.

5 Further analysis and outlook

5.1 Assessing sensitivity to choice of initial conditions

In Section 4.1, we presented estimation results for true sine-generated curves with fixed initial parameters. To further evaluate the sensitivity of the approach to the given initial variance we ran additional tests. We randomly generated 30 pairs of initial variances where $\delta_A, \delta_C, \delta_D \sim \mathcal{U}(0.8, 1.2)$ and $\delta_B \sim \mathcal{U}(0.008, 0.012)$. (These ranges were chosen on the basis of the geological interpretation of these four parameters and, as a result, these meander parameters cover a large portion of all possible rivers on Earth.) The curves in Figs. 12 and 14 show that neither the predictions made by the EKF, nor those of the CIUKF, are sensitive to initial covariance matrices. For UKF, in Fig. 13, the maximum and minimum state weighted error differ by more than 4 magnitudes. The degradation of all estimates using EKF and UKF further support our suggestion that CIUKF is the preferred choice.

5.2 Quantifying confidence in the predictions

The curves in Figs. 4, 6, and 8 show that predictions generally improve with additional measurements, but also that there are parts of river bends that deviate from the sine-generated curve model. In judging curves by sight alone one can easily be mislead. What is desired is a measure of precision with an obvious interpretation: we wish to have a general sense of how useful the resulting

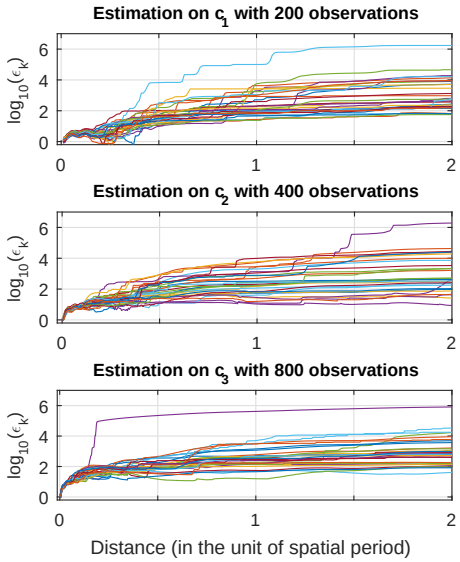

Figure 13: State weighted error of predictions made by the UKF. The horizontal axis is in units of the ground truth curve's spatial period.

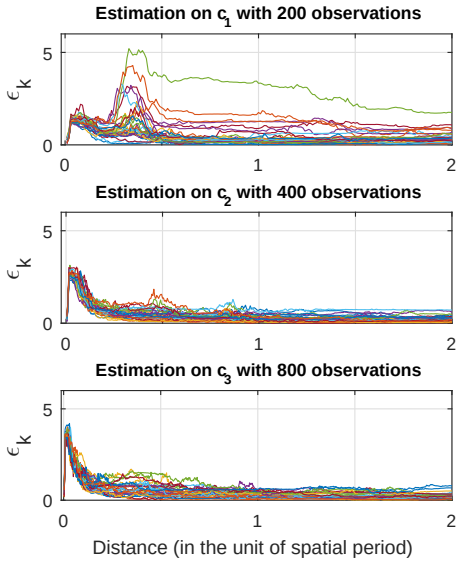

Figure 14: State weighted error of predictions made by the CIUKF. The horizontal axis is in units of the ground truth curve's spatial period.

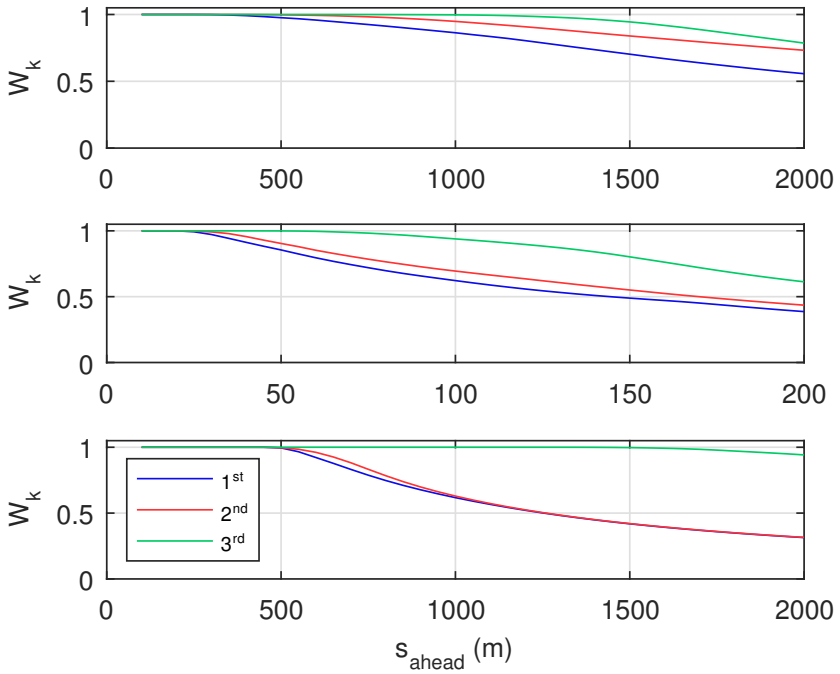

Figure 15: Prediction confidence *vs.* look-ahead distance for the (top) Brazos, (center) L'Anguille, and (bottom) Colorado Rivers. The 1st, 2nd, and 3rd refer to the three positions on meanders shown in Figs. 4, 6 and 8, respectively.

predictions will be for subsequent planning. If the estimator's output is to be used by a robot to select its actions, for example, in bounding throttling speeds as the boat rounds a bend, a metric that relates to some notion of risk as a function of distance ahead of the boat seems prudent.

We introduce a measure, that we call the *prediction confidence*, which serves to quantify that proportion of predictions (weighted by the probability) falls inside the river. The idea is that one can tolerate some imprecision, but misclassifying riverbank for water is crucial mistake. This confidence is most meaningful when thought of as a curve that falls off a one looks further up the river. We define W_k, the prediction confidence at state k, as:

$$W_k(s_{\text{ahead}}) = \int_{-\infty}^{+\infty} \min\left(\frac{s_{\text{in}}}{s_{\text{ahead}}}, 1\right) \Pr\left(x \mid \hat{x}_k, P_k\right) \, \mathrm{d}x, \tag{44}$$

where $\Pr\left(x \mid \hat{x}_k, P_k\right)$ is the probability density of the normal distribution with mean $\hat{x}_k$ and variance P_k, s_{ahead} is the look-ahead distance and s_{in} is how far the look-ahead distance remains inside the riverbanks. The value of s_{in} is computed starting from the Cartesian coordinates of the position at s_k. (Note that, up to this point, the report has considered only the centerline of any river; computation of s_{in} also requires knowledge of the river's breadth.)

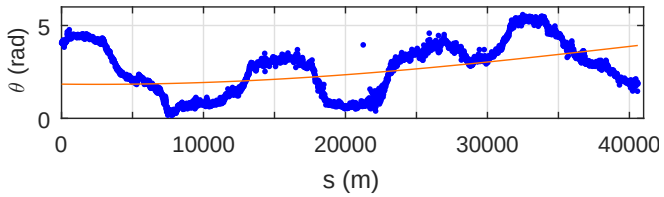

Figure 16: The estimator clearly fails to converge on this long stretch of data, in contrast to successes on local portions of the data. After fusing 4183 measurements, it appears to ignore the 'high-frequency' structure in the angular data.

Fig. 15 shows the prediction confidence versus look-ahead distance for three positions on meanders shown in Figs. 4, 6, and 8. This quantifies the improvement in prediction as the filter processes more observations (from the first location to the second, and to the third), indicating how the robot can have more confidence in its estimation. Analyzing these curves allows one to understand the horizon over which a planner might safely and profitably operate.

5.3 Nonstationarity in the meander model

Following the evaluation reported in Section 4.3, we attempted to run CIUKF on the full homeward trajectory taken by the boat, shown in Fig. 10. The measured and the end-location CIUKF estimated angles are shown in Fig. 16 in a plot similar figures before. In this case, the failure of CIUKF to fit a sinusoidal curve to the measured directional angles is obvious. We posit that this failure is because the overall trajectory of the river is not sufficiently well-characterized with a sine-generated curve for any choice of parameters.

One might have better success on this full trajectory if it is regard as a piecewise concatenation of multiple sine generated curves, each with local sine-generated curves. One may be able to reset the filter once a series of measurements indicate poor fit and converge (from the prior) to a good local characterization. (This is not an entirely idle speculation, as the data in Fig. 9 are very similar to a window in Fig. 16, one being part of the outward journey, the other being the full return journey.) Alternatively, with a better understanding of how non-stationarity is manifest in river meanders, one may be able to capture this in (30). These remain directions for future work.

6 Limitations and issues for future work

This work represents a first examination of how structure induced in rivers by their flowing waters can be exploited to help robots tasked with navigating such waters. We have shown that it certainly is possible to use such structure to help provide reasonable predictions of what lies around the next bend, but the predictions produced are not yet useful for control. For one thing, in watercourses

of the scale used for conducting our evaluation, any ASV would certainly have amble time to react without prediction. At 10 m/s, a reactive control policy would certainly suffice—it remains to be seen whether small craft navigating on narrow channels of water would be able move at sufficient speed to need predictions of this form.

Even if it is not the case that models of rivers based on geological data are directly useful for control, such models can help with planning and other computations operating at slower timescales. Examples include applying such models to infer features of the river for which the riverbank geometry is a useful indicator, such as the *thalweg* (mentioned on pg. 3), and the flow characteristics affected by the shape (but also width) of the river. When additional data, like measurements of how rapidly elevation is changing, and other domain knowledge are fused, the result has the potential to provide rich task-level information.

In Section 5.3 we have discussed the challenges of non-stationarity in the sine-generated curve model. In future work we are interested in examining parameterizations which involve a sum of sinusoids or a composition of a sinusoid and a cubic spline to approximate larger structural properties.

7 Conclusion

In this report, we have shown how to use a simple but classical geological model of watercourses to parameterize estimators. The periodic and non-linear form of the model, while quite natural seeing as river meanders are themselves characteristically periodic phenomena, poses challenges for straightforward Kalman-based filters. Our results provide convincing evidence that imposing state space constraints to ensure unimodality improves the quality of prediction estimates, helping achieve convergence. The model of meanders has been shown to be applicable across an impressive range of scales, from small streams to cross-continental rivers. In our evaluation too, we examine diverse scales of river. When the observations are from a part of the river that is well-described by the meander model, no matter the particular scale of the river, the estimates are sufficient to aid a planner.

More broadly, the regularity induced by a flowing stream of water represents an important opportunity for the roboticist. Relatively little research has incorporated such structure, but the present report provides only one example of a rich lode ready for exploitation.

Acknowledgements

Part of the costs of this research were covered by NSF awards IIS-1302393 and IIS-1453652, support for which we are grateful.

We wish to thank our skipper, John, who used his 30 years of expedience in piloting his trusty ski-boat (see Fig 17) along the Colorado and ensured we

Figure 17: The boat used for data collection, see Section 4.3.

were able to collect good-quality data safely.

Appendix

We provide a proof for the unimodality of the state distribution within the constrained interval $(x_L, x_U]$. Consider two trigonometric functions:

$$\theta_1(s) = A_1 \sin(B_1 s + C_1) + D_1, \tag{45}$$

$$\theta_2(s) = A_2 \sin(B_2 s + C_2) + D_2, \tag{46}$$

where $s \in [0, \infty)$ and if $x_1 = [A_1\ B_1\ C_1\ D_1]^\mathsf{T}$, and $x_2 = [A_2\ B_2\ C_2\ D_2]^\mathsf{T}$, where x_L and x_U are defined in (42). If $x_L < x_1 \leq x_U$ and $x_L < x_2 \leq x_U$, then the unimodality follows when, for all $s \in [0, \infty)$,

$$x_1 \neq x_2 \implies \theta_1(s) \neq \theta_2(s). \tag{47}$$

By rearranging $\theta_1(s) = \theta_2(s)$ we have:

$$A_1 \sin(B_1 s + C_1) - A_2 \sin(B_2 s + C_2) = D_2 - D_1. \tag{48}$$

Here $D_1 = D_2$ because the left-hand side of (48) cannot equal a non-zero constant. Then we write (48) as:

$$A_1 \sin(B_1 s + C_1) = A_2 \sin(B_2 s + C_2). \tag{49}$$

where either $A_1 = A_2 = 0$ (which is prohibited by the lower constraint x_L) or neither. Also $\sin(B_1 s + C_1)$ and $\sin(B_2 s + C_2)$ are non-zero for some s, since

$x_1, x_2 > x_L = [0\ 0\ 0\ 0]^\mathsf{T}$. So by rearranging (49) we have:

$$\frac{A_1}{A_2} = \frac{\sin(B_2 s + C_2)}{\sin(B_1 s + C_1)}. \tag{50}$$

To make the right hand side of the preceding a constant value of $\frac{A_1}{A_2}$, we can get:

$$B_2 s + C_2 = B_1 s + C_1 + k\pi, \qquad \text{or} \tag{51}$$

$$B_2 s + C_2 = -B_1 s - C_1 + k\pi, \qquad k \in \mathbb{Z}, \tag{52}$$

where (52) is prohibited by the positivity of B_1 and B_2. When k is odd, then from (51) we have $A_1 = -A_2$, which is prohibited by the lower constraint x_L. Therefore, k must be even and $A_1 = A_2$. For even k in (51), we obtain $B_1 = B_2$ and $C_2 = C_1 + k\pi$. As $C_1,\ C_2 \in (0, 2\pi]$, we conclude that $C_1 = C_2$. Thus

$$\theta_1(s) = \theta_2(s) \implies x_1 = x_2, \tag{53}$$

and unimodality of the state distribution follows from the contrapositive.

We note that the interval we have taken is *maximal* in possessing the non-periodicity for, if the $x_L < x_k$ constraint is relaxed to $x_L \leq x_k$, then we find there are multiple solutions to and (53) holds no longer.

References

[1] Girish Chowdhary and Ravindra Jategaonkar. Aerodynamic Parameter Estimation from Flight Data Applying Extended and Unscented Kalman Filter. *Aerospace Science and Technology*, 14(2):106–117, March 2010.

[2] Albert Einstein. Die Ursache der Mä anderbildung der Flußläufe und des sogenannten Baerschen Gesetzes. *Die Naturwissenschaften*, 14, 1926. English translation "The Cause of the Formation of Meanders in the Courses of Rivers and of the So-Called Baer's Law" at `http://people.ucalgary.ca/~kmuldrew/river.html`.

[3] Simon Julier, Jeffrey Uhlmann, and Hugh F. Durrant-Whyte. A new method for the nonlinear transformation of means and covariances in filters and estimators. *IEEE Transactions on Automatic Control*, 45(3):477–482, March 2000.

[4] Luna B. Leopold and Walter B. Langbein. River Meanders. *Scientific American*, 214:60–70, 1966.

[5] Daniel E. Mecklenburg and Anand D. Jayakaran. Dimensioning the Sine-Generated Curve Meander Geometry. *Journal of the American Water Resources Association*, 48(3):635–642, February 2012.

[6] Michael J. Quinlan and Richard H. Middleton. Multiple Model Kalman Filters: A Localization Technique for RoboCup Soccer. In *Robot Soccer World Cup*, volume 5949, pages 276–287. Springer, Lecture Notes in Computer Science, 2009.

[7] Daniel J. Simon. Kalman filtering with state constraints: a survey of linear and nonlinear algorithms. *IET Control Theory & Applications*, 4(8):1303–1318, August 2010.

[8] Franklin D. Snyder, Daniel D. Morris, Paul H. Haley, Robert T. Collins, and Andrea M. Okerholm. Autonomous River navigation. In *Proceedings of SPIE, Mobile Robots XVII*, volume 5609, pages 221–232, December 2004.

[9] Bruno O. S. Teixeira, Leonardo A. B. Tôrres, Luis A. Aguirre, and Dennis S. Bernstein. Unscented filtering for interval-constrained nonlinear systems. In *IEEE Conference on Decision and Control*, pages 5116–5121, December 2008.

[10] T. R. Thakur and Adrian E. Scheidegger. A test of the statistical theory of meander formation. *Water Resources Research*, 4(2):317–329, April 1968.

[11] Sebastian Thrun, Wolfram Burgard, and Dieter Fox. *Probabilistic Robotics*. MIT press, 2005.

[12] Pramod Vachhani, Shankar Narasimhan, and Raghunathan Rengaswamy. Robust and reliable estimation via Unscented Recursive Nonlinear Dynamic Data Reconciliation. *Journal of Process Control*, 16(10):1075–1086, December 2006.

[13] Pramod Vachhani, Raghunathan Rengaswamy, Vikrant Gangwal, and Shankar Narasimhan. Recursive estimation in constrained nonlinear dynamical systems. *American Institute of Chemical Engineers (AIChE) Journal*, 51(3):946–959, February 2005.